

Analysis and modeling of the high vacuum scanning spreading resistance microscopy nanocontact on silicon*

Pierre Eyben,^{a)} Francesca Clemente, Kris Vanstreels, Geoffrey Pourtois, Trudo Clarysse, Edouard Duriau, and Thomas Hantschel
IMEC vzw, Kapeldreef 75, B-3001 Leuven, Belgium

Kiroubanand Sankaran
IMEC vzw, Kapeldreef 75, B-3001 Leuven, Belgium and Unité PCPM-UCL, Croix du Sud, 1; B-1348 Louvain-la-Neuve, Belgium

Jay Mody and Wilfried Vandervorst
IMEC vzw, Kapeldreef 75, B-3001 Leuven, Belgium and Instituut voor Kern-en Stralingsfysika, K.U. Leuven, Celestijnenlaan 200D, B-3001 Leuven, Belgium

Kausala Mylvaganam and Liangchi Zhang
Center for Advanced Materials Technology, University of Sydney, New South Wales 2006, Australia

(Received 13 July 2009; accepted 19 October 2009; published 30 March 2010)

Within this paper, the authors propose a refined high vacuum scanning spreading resistance microscopy (HV-SSRM) electromechanical nanocontact model based on experimental results as well as molecular dynamics (MD) simulation results. The formation under the tip of a nanometer-sized pocket of β -tin, a metastable metalliclike phase of silicon (also named Si-II), acting as a virtual probe is demonstrated. This gives a reasonable explanation for the superior SSRM spatial resolution as well as for the electrical properties at the Schottky-like SSRM contact. Moreover, the impact of the doping concentration on the plastic deformation of silicon for different species using micro-Raman combined with indentation experiments is studied. In order to elucidate the superior results of SSRM measurements when performed under high vacuum conditions, the impact of humidity on the mechanical deformation and Si-II formation is also analyzed using MD and SSRM experimental results. © 2010 American Vacuum Society. [DOI: 10.1116/1.3273895]

I. INTRODUCTION

Scanning spreading resistance microscopy (SSRM) is an atomic force microscope-based technique (see Fig. 1) that has been developed in the recent years to characterize the two-dimensional (2D) carrier distributions in semiconductor devices.^{1,2} In SSRM, a conductive tip is used to probe the local resistivity (linked to the net carrier concentration) via the acquisition of the related spreading resistance.³ Using high vacuum scanning spreading resistance microscopy (HV-SSRM) combined with molded full diamond tips,⁴ we have recently achieved subnanometer spatial resolution and an excellent signal to noise ratio.^{5,6}

The main purpose of our work is to investigate at the atomistic level the mechanical and electrical properties of the SSRM nanocontact. We try to understand how subnanometer spatial resolution can be obtained when probing the surface of interest with a conductive diamond tip having a relatively large radius of curvature (5–15 nm) as seen in a scanning electron microscopy (SEM). We show that the mechanical deformation and resulting Si-structure are of fundamental importance relative to the electrical contact properties of SSRM.

II. STUDY OF THE HV-SSRM MECHANICAL NANOCONTACT USING MOLECULAR DYNAMICS SIMULATIONS

In previous work,⁷ finite element method (FEM) simulations were performed to study the impact of the diamond tip on silicon during SSRM measurement process (corresponding to a large pressure indentation). These results have shown the possibility to obtain metastable β -tin pockets under the SSRM tip that have a much smaller radius than the radius of curvature of the tip. Validity and accuracy of FEM simulations results for stress distributions in the nanometer-range should, however, be regarded with a lot of cautiousness.

Hence we present more refined calculations using molecular dynamics (MD) simulations. MD method is a powerful tool for investigating the deformation of silicon under nanoindentation and the formation of new silicon crystallographic phases and, in particular, metastable phases such as β -silicon and BCT5-silicon.^{8–10} Within this work, we have used MD as a support to analyze the SSRM nanocontact. For further details on MD, please note the intensive studies of Mylvaganam *et al.*,¹¹ Zhang and Tanaka,¹² and Cheong *et al.*⁸

In order to validate the radius of curvature estimated with SEM, high resolution (atomic) transmission electron microscopy (TEM) inspection of the tip apex was performed. A TEM analysis was performed on both pristine (Fig. 2, left)

*This paper was presented at the International Workshop on INSIGHT in Semiconductor Device Fabrication, Metrology and Modeling (INSIGHT-2009) convened April 26–29, 2009 in Napa, California.

^{a)}Electronic mail: pierre.eyben@imec.be

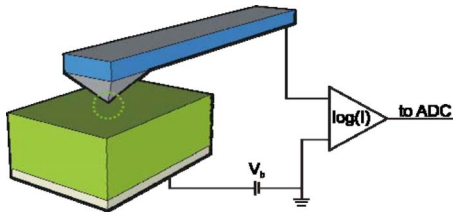


FIG. 1. (Color online) Experimental setup of the SSRM technique.

and used tips (Fig. 2, right corresponding to a tip used in scan mode and presenting a good spatial resolution). The TEM inspection reveals that the molded diamond tips used in our experiments⁴ were undergoing an initialization mechanism. As can be seen in Fig. 2, nanoprotusions of diamond are present at the extremity of the initialized tip. We speculate that due to the shear forces, nondiamond parts (such as silicon carbide) at the outer surface of the molded tip (corresponding to the first layers grown during the diamond deposition) are most probably removed while the tip is scanned across the silicon sample (initialization process). It is not yet completely clear whether simple contact indents could be sufficient to initialize the tip or if scanning (implying the presence of a large shear stress) is needed. In previous work,¹¹ we have been able to establish one-to-one correlations between SSRM measurements in point-contact mode and MD simulations with an indent presenting a radius of curvature of 7.5 nm. This tends to prove that scanning may be needed to initialize the tips. Present results are based on the analysis of two different used tips and additional statistics are likely needed to validate this model more conclusively. Moreover it would also be interesting to evaluate how much the radius of curvature of unused and initialized tips can vary from tip to tip. These studies are hampered by the special TEM-sample preparation procedure required for these tips.

Mylvaganam *et al.*¹¹ recently discovered that under equivalent indentation loads, MD predictions agree extremely well with the experimentally measured result by SSRM, in terms of the depth of the residual indentation marks and the onset, evolution, and dimension variation of the metastable phases, such as Si-II (or β -tin Si). A new six-coordinated silicon phase, Si-XIII, transformed directly from Si-I was also discovered. Their investigation also identified that the Si-II and the Si-XIII phases are surrounded by a five-coordinated phase [BCT5-Si (Ref. 10)]. Within this

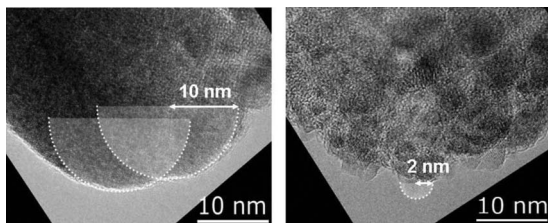


FIG. 2. TEM pictures of the apex of unused (left) and initialized (right) full diamond tips.

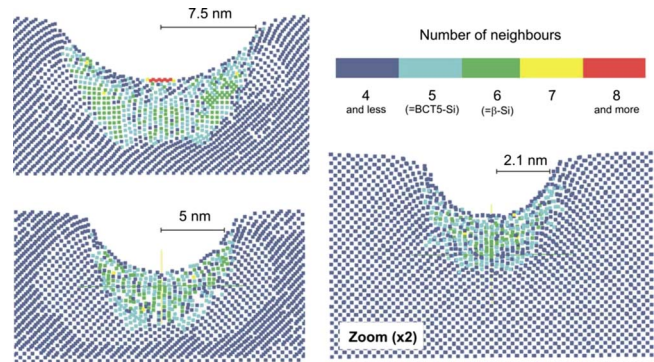


FIG. 3. (Color online) Cross-sectional view of the location of atoms at the maximum indentation depth for radii varying between 7.5 and 2.1 nm. The different colors do correspond to the amount of neighbors for every atom. The β -tin does correspond to the atoms in dark grey. Note that these results are from Ref. 11.

work we focused on $\langle 100 \rangle$ silicon sample indented using hemispherical diamond tips with a radius varying between 2 and 10 nm to match with the radius of curvature observed with TEM for both unused and initialized tips. The MD method allows the simulation of the phase transition without any assumption on the nature of the phases. The resulting structures only depend on the thermomechanical conditions and on the interaction forces between atoms, as defined by the potential function.

To avoid boundary effects, large silicon samples were used. Boundary atoms and thermostat atoms were arranged to surround the Newtonian atoms of silicon to eliminate the rigid body motion and to conduct heat.^{8,12} Interactions among silicon atoms were described by the Tersoff potential^{13,14} and among silicon and diamond atoms were described by a modified Morse potential, as explained elsewhere.¹²

As the different phases involve a different number of Si atoms interacting with each other, we plot the three-dimensional (3D) distribution of Si atoms as a function of the number of nearest neighbors (coordination number). As a criterion to define a neighboring atom we look for Si atoms whose interatomic distances are less than 2.58 Å.^{8,15} In Fig. 3, a 2D section through the center of the indenter is presented for indenters with a radius of curvature of 7.5, 5, and 2.1 nm, respectively. One can observe that during indentation, a part of the diamond cubic silicon (with a localized sp^3 molecular orbital) is transformed into different high-pressure phases: one phase with six nearest neighbors (Si-II, known as β -tin Si and Si-XIII, with an sp^3d^2 molecular orbital in which d^2 is corresponding to nonlocalized electrons leading to a metalliclike behavior), and one phase with five neighbors and known as BCT5-silicon (with an sp^3d^1 molecular orbital and thus also nonlocalized electrons). These metastable phases¹⁰ both have a metallic body-centered tetragonal structure, β -silicon being known to be the more conductive.

Given the 3D distribution of the atoms obtained from the MD approach, we have calculated the stress (hydrostatic, biaxial, and uniaxial) that every atom was undergoing. The computation of the different stresses and their distribution

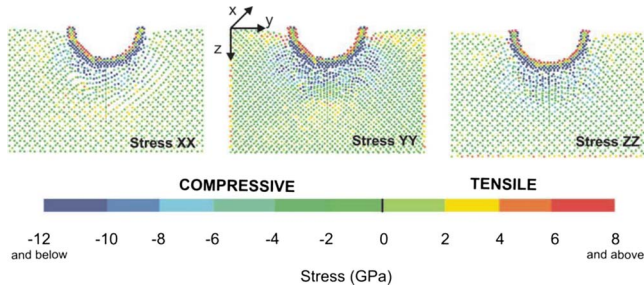


FIG. 4. (Color online) Cross-sectional view of the location of atoms at the maximum indentation depth for an indenter with a radius of curvature of 2.1 nm. The different colors do correspond to the different stress levels in XX, YY, and ZZ directions.

has been performed based on the forces^{8,12,16,18} and on the atomic energy generated by the pair potentials of Tersoff.^{14,17,18}

As mentioned by Shen and Chen,¹⁹ the interpretation of the virial stress as a measure for mechanical force violates balance of momentum. The interatomic force alone is a valid stress measure and can be identified with the Cauchy stress. In this study, the formulations employed to calculate atomic-level stress are motivated by the above considerations. At each atom, the local stress tensor, β_i , is given by

$$\beta_i = \frac{1}{\Omega_i} \sum_{j \neq i}^N f_{ij} \otimes \vec{r}_{ij},$$

where i refers to the atom considered, j refers to the neighboring atom, \vec{r}_{ij} is the position vector between atoms i and j , N is the number of neighboring atoms surrounding atom i , Ω_i is the volume of atom i (note that the volume is computed based on a spherical model whose radius is defined based on a close-neighbor list analysis), and f_{ij} is the force vector on atom i due to atom j determined as the gradient of potential energy, namely,

$$f_{ij} = -\frac{\vec{r}_{ij}}{r_{ij}} \left(\frac{dV(\vec{r}_{ij})}{dr_{ij}} \right),$$

where r_{ij} is the distance between atoms i and j , and $V(\vec{r}_{ij})$ is the potential energy between atoms i and j . Note that β_i is the stress tensor defined at atom i , while the global continuum stress tensor is defined as a volume average, namely,

$$\sigma = \frac{1}{N^*} \sum_i \beta_i,$$

in which N^* represents the total number of active atoms in a representative volume of continuum.

Figure 4 shows the atomic stress calculated using this formalism along the three main directions (XX, YY, and ZZ from top to bottom). Just below the indenter, in the central part, relatively large compressive stresses can be observed in all three directions.

To visualize more easily the nature of the stress, a small routine has been written in order to discriminate atoms undergoing stress that is mainly uniaxial, biaxial, or triaxial

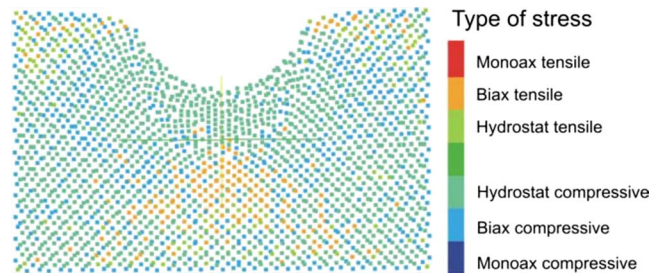


FIG. 5. (Color online) Cross-sectional view of the location of atoms at the maximum indentation depth for a radius of 2.1 nm. The different colors do correspond to the different kinds of stress dominating.

(further referred to hydrostatic even if it is not a purely hydrostatic stress). In Fig. 5, one can see that the stress directly under the indenter (not only in the central part but along the whole tip-silicon interface) is hydrostatic and compressive which leads to bandgap narrowing and thus to a more carrier populated area.²⁰ Note that biaxial tensile stress is observed further below the indenter.

III. TOWARD AN ELECTROMECHANICAL NANOCONTACT MODEL FOR HV-SSRM

A first SSRM electromechanical model was proposed by Eyben *et al.* in Ref. 21. Within this model, the SSRM nanocontact on silicon is represented as the juxtaposition of three different zones: (1) the diamond tip (or diamond indenter), (2) the Si-II metalliclike metastable phase of silicon, and (3) the silicon to be analyzed (that is elastically deformed).

The contact between the highly B-doped diamond tip and the Si-II pocket could be considered as Ohmic due to the metallic nature of the Si-II pocket region. Its contribution to the contact resistance is thus marginal. Hence, the SSRM nanocontact is dominated by the Si-II–Si-I contact which is a metal-semiconductor (or Schottky) contact. The exact nature of this electrical nanocontact (including impact of tunneling current through the barrier and influence of surface states) has been described and successfully modeled and simulated elsewhere.²¹

The MD results from Mylvaganam *et al.*¹¹ (Fig. 3) confirm this model and identify the presence of an extra metastable phase (BCT5-Si). It is still unclear how the current flows from the tip to the Si-I through BCT5-Si, the Si-II, and the Si-XIII. We, however, believe that most of the current will flow through the “more metallic” β -Si pocket due to its high conductivity.

Using the MD results, we can also look at the SSRM spatial resolution. The extreme resolution obtained with SSRM (subnanometer in high vacuum) tends to indicate that the current measured is spreading through an extremely localized position, sensing the resistivity of a very small silicon volume. Based on the previous FEM simulations, we speculated that the high resolution of SSRM was directly linked to the size of the β -tin region formed underneath the tip. The results presented here (see Fig. 3) confirm that this concept as the β -tin pocket has indeed a radius of curvature (around 1–1.5 nm) similar to the 2–3 nm spatial resolution

and much smaller than the tip radius (2.1 nm). The β -tin pocket size presented in Fig. 3 corresponds to the largest indentation depth and could slightly diminish when the indentation force is reduced.

We also believe the superior resolution of SSRM is additionally linked to an extra constriction of the current flow linked to the bandgap narrowing (current will most probably follow the smallest bandgap pathway). Further investigations are needed to allow more detailed considerations but we believe that the current will be confined at the central part of the indent before its spread in Si-I.

A last factor that could explain the high resolution is the fact that the β -tin pocket could be reduced while operating in sliding mode (what is corresponding to an SSRM scan) rather than in point contact mode.²²

IV. IMPACT OF DOPING CONCENTRATION

HV-SSRM is performed over devices with doping concentrations typically varying between 10^{15} and 10^{20} at./cm³ for both *p*- and *n*-type dopants. It is therefore crucial to analyze the impact of the doping concentration on the plastic deformation of silicon and, in particular, on the formation of β -tin Si and thus to assess any concentration dependent resolution. A study of Yan *et al.*²³ based on the micro-Raman spectrometer analysis of nanoindented (111) silicon samples showed that boron doping was significantly enhancing the formation of amorphous silicon (*a*-Si). This tends to indicate an enhanced formation of metastable β -tin (that is transformed into *a*-Si when the pressure is released) for heavily boron doped silicon when it is indented. This hypothesis is in good agreement with our experimental observations. Measuring with SSRM on highly doped silicon, one can indeed obtain a stable and low resistive electrical contact at lower force as compared to lowly doped silicon. As a consequence, assuming that the final spatial resolution is mainly determined by the size of the β -tin pocket (previous results, however, tend to prove that this may not be fully the case as another metalliclike metastable phase is present), this could lead to a dopant concentration dependence of the spatial resolution. For a similar indentation force, heavily boron doped silicon areas would indeed present a larger metastable β -tin pocket as compared to lowly doped areas. The underlying mechanism is most probably linked to the large atomic size difference between boron and silicon, as well as to the reduction in the shear elastic constant caused by the boron doping. As a consequence, also different dopant species (B versus As) may have a different impact on the β -tin formation.

Experiments similar to the one described in Ref. 23 were performed on lowly and heavily doped pieces of (100) silicon for both boron (P1 \sim 0.01 Ω cm and P6 \sim 10.1 Ω cm) and arsenic (N1 \sim 1.03 Ω cm and N5 \sim 10.6 Ω cm) dopant species. We used a nano-indenter system (MTS Systems Corporation) equipped with a Berkovich diamond indenter at constant load/unload rate of 0.8 mN/s and with maximum load of 60 mN. Our first experimental results are qualitatively in good agreement with the one of Yan *et al.* (see Fig. 6). They moreover demonstrate that the behavior for arsenic

doped samples is similar to the one for boron doped samples. A pop-out mechanism (corresponding to volume expansion during the phase transformation of the metastable Si-II) is systematically observed when unloading the samples.²⁴ From Fig. 6, we can also observe that the pop-out occurs at slightly lower pressure for heavily doped silicon for both boron and arsenic species. Note that the fact that both boron (smaller than Si) and arsenic (larger than Si) doped samples present the same behavior tends to attest that the size of the doping atoms is not an important parameter. The pressure reduction observed here is however relatively marginal [0.1–0.2 GPa what is smaller than the one observed by Yan *et al.* for (111) Si]. Moreover, the results present a relatively large variability. These results (that are however in good agreement with experimental results) therefore have to be confirmed and regarded with caution. Considering that pop-in (transformation from Si-I to Si-II) and pop-out mechanisms are linked, one can conclude from Fig. 6 that the formation of β -tin silicon will also occur at slightly lower pressures for heavily doped materials. This is confirmed using micro-Raman analysis (see Fig. 7 for *p*-type) performed in backscattering geometry with a LabRAM HR, using an excitation wavelength of 532 nm focused with a 100 \times objective and a power on the sample was 0.2 mW. From Fig. 7, we can observe that typical micro-Raman graph for high boron doping (within an indent made with the nano-indenter) presents a smaller Si-I peak as compared to the one for low boron doping. This tends to attest that the plastic deformation is enhanced when the boron doping is increased. A similar phenomenon has been observed for arsenic but it is less pronounced.

V. IMPACT OF HIGH VACUUM

When performed in high-vacuum, SSRM is presenting three remarkable improvements as compared to SSRM in air: (1) the signal to noise level is improved, (2) the measurement force is reduced (by a factor 2–4), and (3) the spatial resolution is improved (subnanometer versus 1–3 nm in air).

The signal to noise ratio improvement could be understood fairly intuitively: When measuring in high-vacuum, the presence of organic contaminants is drastically reduced and there is no water film at the surface of the sample. The sample oxidation at room temperature (driven by the water in air) is also eliminated. As a consequence, the electrical contact is much more intimate (no nonconductive layer between the tip and the sample) and stable.

Concerning the reduction in the optimal measurement force in HV-SSRM, Tang *et al.*²⁵ have demonstrated, using MD, that in the presence of water (as in air), the growth of β -silicon was retarded (see Fig. 8, left). They explained that this was due to the local stress distribution change caused by the trapped water at the indenter-silicon interface. This could elucidate why we have to exert a higher force to obtain a good (low resistive and low noise) electrical contact when performing SSRM in air. The retardation obtained with MD however remains relatively limited as compared to experimental results. For a refined analysis, performing MD in the presence of water in sliding mode would be interesting.

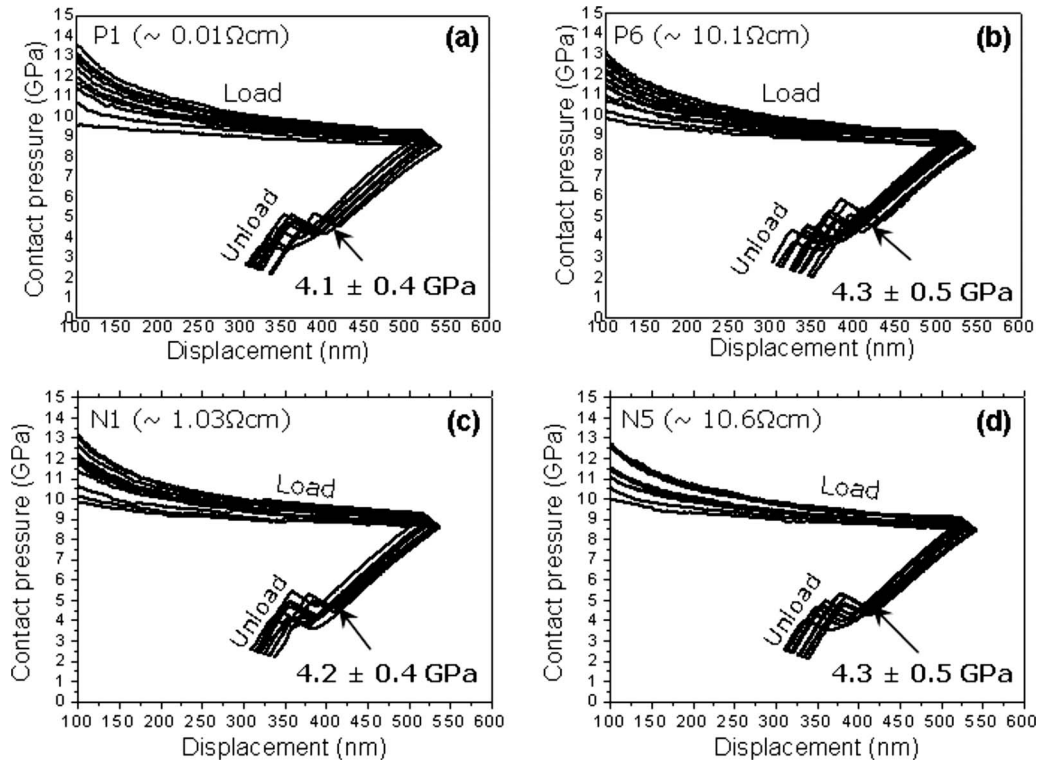


FIG. 6. Pressure displacement curves measured with nano-indenter for highly boron (a) and arsenic (c) doped homogeneous samples as well as for lowly boron (b) and arsenic (d) doped samples.

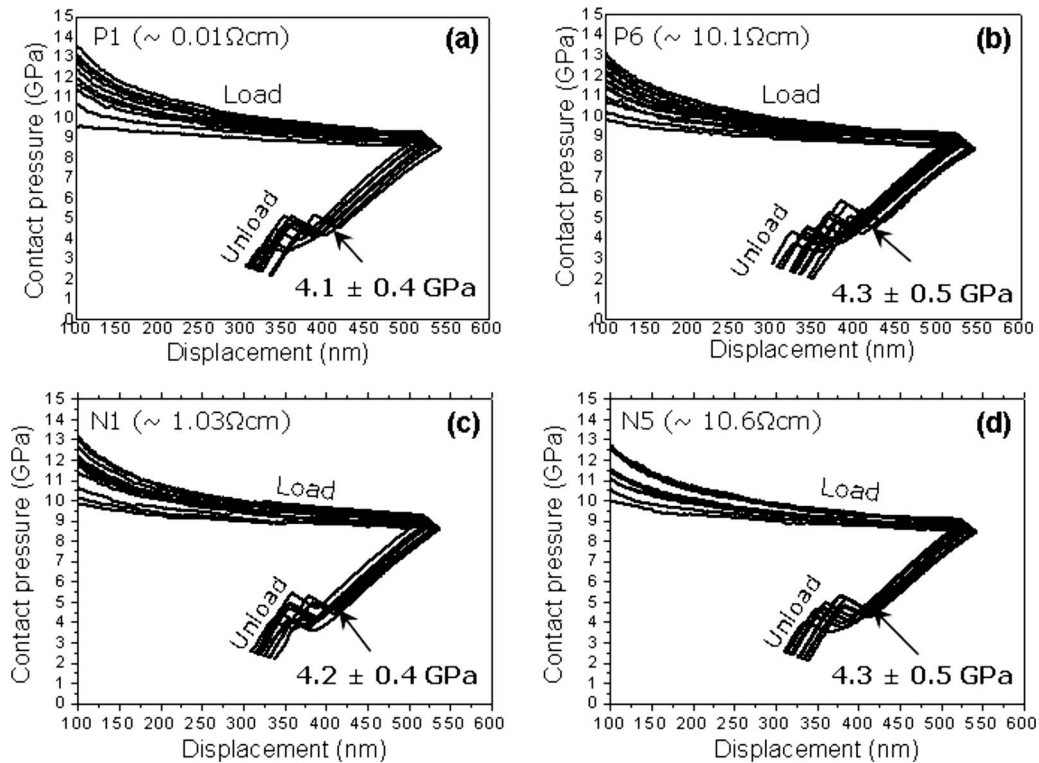


FIG. 7. Typical micro-Raman graphs within the indented areas for highly (left) and lowly (right) boron doped samples. The Si-I Raman peak is smaller for highly doped material indicating more plastic deformation.

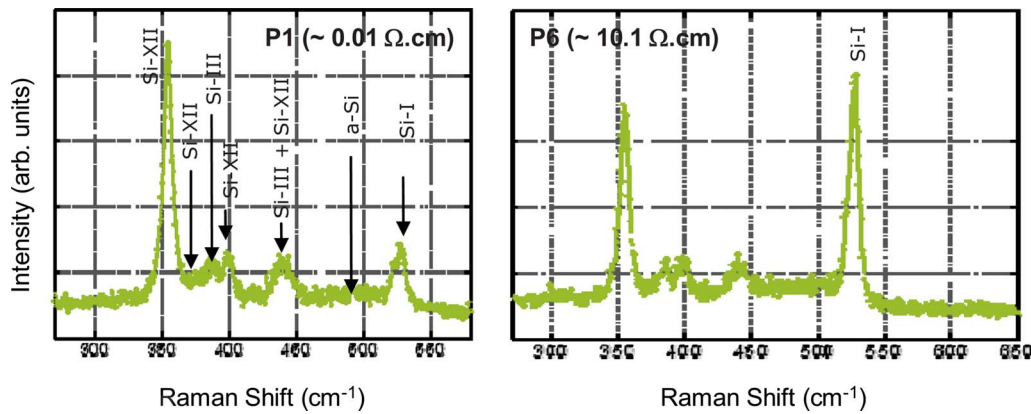


FIG. 8. (Color online) (Left) Structural changes of the substrate during nanoindentation with and without water. (Right) Number of transformed silicon atoms with and without water during loading and unloading (the transformed zone is defined as the zone where the diamond cubic structure has transformed into other structures as well as atoms highly dislocated from their original positions). Note that these results are from Ref. 25.

Moreover, in air, the presence of a native oxide (that is partially regrowing in between two scans) may also play a certain role, acting as a damping layer.

Regarding the lower SSRM spatial resolution in air, from Ref. 25 it is shown that in the presence of water, the volume of the transformed silicon is higher (see Fig. 8, right). This can be explained by the fact that during the loading, water molecules behave as tiny moving surface indenters which penetrate into the silicon surface and modify the stress field in their neighborhood, thereby increasing the number and volume of the transformed silicon atoms. A similar abrasive mechanism has been demonstrated for silicon nanoindentation in the presence of oxygen molecules.²⁶

VI. CONCLUSION

The MD results from Mylvaganam *et al.*¹¹ and Tang *et al.*²⁵ have been used to analyze the SSRM nanocontact at the atomic level. The MD results match nicely with the experimental SSRM observations and confirm the electromechanical SSRM nanocontact model.²¹ The presence of another metastable phase (BCT5-Si) is revealed.

The role of doping concentration on the β -silicon formation has been studied. For high doping concentrations (for both B and As), we observe an enhancement of *a*-Si formation as well as a slight reduction in the pop-out pressure. We believe that this is an indication for the formation of a larger β -tin pocket for the same indenting force and for a reduction in the force needed to plastically deform silicon. This effect is however relatively limited.

Finally, using MD results²⁵ we have also been able to explain the superior performance of HV-SSRM as compared to classical SSRM in air. In particular, the role of water, acting as β -tin formation retarder and enhancer, has been evidenced.

ACKNOWLEDGMENTS

The authors would like to acknowledge O. Richard, P. Van Marcke, and H. Bender for supplying the TEM results,

as well as C. Demeulemeester for the diamond tip fabrication. K.M. and L.C.Z. appreciate the financial support from the Australian Research Council to the research.

¹P. De Wolf, J. Snauwaert, T. Clarysse, W. Vandervorst, and L. Hellemans, *Appl. Phys. Lett.* **66**, 1530 (1995).

²P. Eyben, W. Vanservorst, D. Alvarez, M. Xu, and M. Fouchier, *SPM: Electrical and electromechanical phenomena at the nanoscale* (Springer, New York, 2007), Chap. I.2.

³P. Eyben, M. Xu, N. Duhayon, T. Clarysse, S. Callewaert, and W. Vandervorst, *J. Vac. Sci. Technol. B* **20**, 471 (2002).

⁴T. Hantschel, P. Niedermann, T. Trenkler, and W. Vandervorst, *Appl. Phys. Lett.* **76**, 1603 (2000).

⁵L. Zhang, K. Ohuchi, K. Adachi, K. Ishimaru, M. Takayanagi, and A. Nishiyama, *Appl. Phys. Lett.* **90**, 192103 (2007).

⁶P. Eyben, J. Mody, and W. Vandervorst, (unpublished).

⁷P. Eyben, D. Degryse, and W. Vandervorst, *AIP Conf. Proc.* **788**, 264 (2005).

⁸W. C. D. Cheong and L. C. Zhang, *Nanotechnology* **11**, 173 (2000).

⁹D. E. Kim and S. I. Oh, *Nanotechnology* **17**, 2259 (2006).

¹⁰D. E. Kim and S. I. Oh, *J. Appl. Phys.* **104**, 013502 (2008).

¹¹K. Mylvaganam, L. C. Zhang, P. Eyben, J. Mody, and W. Vandervorst, *Nanotechnology* **20**, 305705 (2009).

¹²L. C. Zhang and H. Tanaka, *JSME Int. J., Ser. A* **42**, 546 (1999).

¹³J. Tersoff, *Phys. Rev. Lett.* **56**, 632 (1986).

¹⁴J. Tersoff, *Phys. Rev. B* **39**, 5566 (1989).

¹⁵C. F. Sanz-Navarro, S. D. Kenny, and R. Smith, *Nanotechnology* **15**, 692 (2004).

¹⁶W. C. D. Cheong and L. C. Zhang, *Key Eng. Mater.* **233–236**, 603 (2003).

¹⁷J. Tersoff, *Phys. Rev. Lett.* **61**, 2879 (1988).

¹⁸J. Tersoff, *Phys. Rev. B* **37**, 6991 (1988).

¹⁹L. Shen and Z. Chen, *Modell. Simul. Mater. Sci. Eng.* **12**, 347 (2004).

²⁰I. Goroff and L. Kleinman, *Phys. Rev.* **132**, 1080 (1963).

²¹P. Eyben, S. Denis, T. Clarysse, and W. Vandervorst, *Mater. Sci. Eng., B* **102**, 132 (2003).

²²L. C. Zhang and H. Tanaka, *Tribol. Int.* **31**, 425 (1998).

²³X. Q. Yan, X. M. Huang, S. Uda, and M. W. Chen, *Appl. Phys. Lett.* **87**, 191911 (2005).

²⁴J. E. Bradby, J. S. Williams, and M. V. Swain, *Phys. Rev. B* **67**, 085205 (2003).

²⁵C. Y. Tang and L. C. Zhang, *Nanotechnology* **16**, 15 (2005).

²⁶K. Mylvaganam and L. C. Zhang, *Nanotechnology* **13**, 623 (2002).